# Robotic Manipulation of Sperm as a Deformable Linear Object

Changsheng Dai, *Member, IEEE*, Guanqiao Shan, *Graduate Student Member, IEEE*, Hang Liu, Changhai Ru, and Yu Sun, *Fellow, IEEE*

***Abstract*—The robotic manipulation of deformable linear objects is a classic and challenging topic. Apart from synthetic objects, such as wires and cables, linear objects are also commonly found in biological cells and organisms. Biomanipulation of such objects is hampered by difficulties, such as limited degrees of freedom of micromanipulators and varied mechanical properties of the biological entities to manipulate. This article presents a robotic manipulation of human sperm, which are deformable cells with a linear shape. The shape and movement of the cell are recapitulated by our developed geometric and kinematic models. Under unfixed constraints between the end-effector and the cell, path planning is designed to update the manipulation point to control cell deformation. A state transition function is formulated in path planning to handle the stiffness variations of sperm without force sensing. A model-predictive controller is designed to minimize the orientation error and manipulation path length. To detect sperm tail for visual feedback, an accuracy of 98% was achieved via deep neural networks. The robotic manipulation of human sperm was performed using a standard clinical setup of a glass micropipette to rotate a sperm to the target orientation. Experimental results showed that robotic sperm rotation achieved an orientation error of 0.8°, a tail curvedness of 0.14 $\mu m^{-1}$, and an operation time of 5.6 s, all significantly less than those of the manual approach. The less orientation error and tail curvedness after robotic rotation led to a significantly lower speed of sperm entering the micropipette during sperm aspiration, resulting in a higher success rate of 97% (versus 76% after manual rotation) for aspiration control.**

***Index Terms*—Cell manipulation, deformable object manipulation, robot.**

Manuscript received 20 January 2022; accepted 5 March 2022. Date of publication 23 March 2022; date of current version 4 October 2022. This work was supported in part by the Natural Sciences and Engineering Research Council of Canada and in part by the Canada Research Chairs Program. This article was recommended for publication by Associate Editor L. Zhang and Editor A. Menciassi upon evaluation of the reviewers' comments. *(Corresponding author: Yu Sun.)*

Changsheng Dai, Guanqiao Shan, Hang Liu, and Yu Sun are with the Department of Mechanical and Industrial Engineering, University of Toronto, Toronto, ON M5S 3G8, Canada (e-mail: changsheng.dai@mail.utoronto.ca; gq.shan@mail.utoronto.ca; drhang.liu@mail.utoronto.ca; sun@mie.utoronto.ca).

Changhai Ru is with the School of Electronic and Information Engineering, Suzhou University of Science and Technology, Suzhou 215009, China (e-mail: rchhai@163.com).

This article has supplementary downloadable material available at https://ieeexplore.ieee.org, provided by the authors. The material consists of a video, viewable with Windows Media Player, showing robotic manipulation of sperm as a deformable linear object. The video shows that human sperm was robotically rotated to the target orientation using a standard clinical setup of a glass micropipette. To deal with large variance of sperm tails in shape and dimension, deep neural networks were developed for robust tail detection. With the intrinsic challenges in cell manipulation, such as micromanipulator's limited degrees of freedom and cell's varied mechanical parameters, mathematical modeling and path planning strategies were developed to rotate a sperm to the target orientation. A state transition function was formulated to update the manipulation point based on sperm tail's deformation behavior. A model-predictive controller was designed to minimize the orientation error and manipulation path length.

This article has supplementary material provided by the authors and color versions of one or more figures available at https://doi.org/10.1109/TRO.2022.3158200.

Digital Object Identifier 10.1109/TRO.2022.3158200

## I. Introduction

THE robotic manipulation of deformable linear objects has applications, such as knotting ropes [1], manipulating cables [2], and suturing wires [3]. Different from rigid body manipulation, the manipulation of deformable objects requires their deformation behavior to be taken into account. Moreover, deformable objects in theory have infinitive degrees of freedom (DOFs); thus, the manipulation of these objects is highly underactuated given the limited DOF of manipulators [4].

Biological entities are deformable, and a number of cells and organisms exhibit linear shapes, such as sperm, worms (C. elegans), and zebrafish [see Fig. 1(a)–(c)], to name a few. The linear shape endows these cells and organisms with hydrodynamic advantages for movement [5]. Manipulating cells and organisms with a linear shape has many biomedical and clinical applications. For instance, the adjustment of position and orientation of C. elegans into a desire pattern (e.g., parallel array) is required for phenotypic analysis [6], [7]. In clinical infertility treatment [8], a sperm needs to be immobilized by tapping its tail with a glass micropipette [see Fig. 1(d)] and, then, aspirated into the micropipette for deposition into an oocyte [see Fig. 1(f)] for fertilization.

In sperm immobilization, a target sperm is selected with its tail vertical to the micropipette to prevent tapping the sperm head where genetic materials are contained [see Fig. 1(e)]. Before aspirating the immobilized sperm into the micropipette, the sperm tail needs to be rotated to be coaxial with the micropipette [see Fig. 1(g)]. Since the tail is deformable, the deformation along the sperm tail needs to be controlled to minimize the tail's curvedness. When the sperm tail is not coaxial with the micropipette, it takes a higher flow rate to aspirate the sperm since the flow rate attenuates when deviating from the micropipette axis. Aspiration under a high flow rate risks losing the sperm when the sperm rapidly enters and travels deeply into the micropipette. Thus, the manipulation task is to rotate the sperm tail to be coaxial with the micropipette and minimize the tail curvedness.

Presently, sperm tail rotation is performed manually by pushing the sperm tail with the micropipette, which is a trial-and-error

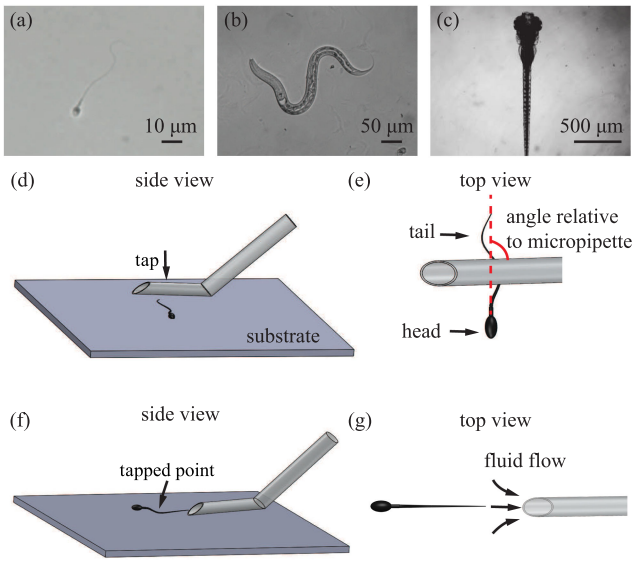


Fig. 1. Biological organisms with a linear shape: (a) human sperm, (b) C. elegans, and (c) zebrafish. (d) In sperm immobilization, a sperm tail needs to be vertical to the micropipette to prevent tapping sperm head where DNA is contained. (e) Side view of sperm immobilization. The sperm is immobilized by tapping its tail with a micropipette. (f) Before aspirating the immobilized sperm into the micropipette, the sperm tail must be rotated to be coaxial with micropipette. (g) Top view of sperm aspiration.

process. Manual manipulation also decreases the fertilization potential of sperm because after immobilization. The tail membrane is broken to release phospholipase C zeta (PLC$\zeta$) for oocyte activation [9], and higher time cost of manual manipulation reduces the amount of PLC$\zeta$ left within the tail [10].

Robotic cell manipulation has gained significant advance, with applications in cell transportation [11], characterization [12], and surgery [13]. To achieve cell rotation, several robotic strategies have been developed. Fluid flow was induced by pressure [14] or vibration [15] to rotate mouse embryos; however, the accuracy was susceptible to flow inertia and cell position in the fluid flow field. Dielectrophoretic forces were employed to rotate cells, but the effect of the applied electrical field on cell development requires further investigation [16]. Optical tweezers were used for cell rotation by applying focused laser beam on a cell [17], but involved risks of photodamage to the cell [18]. Microscope rotational stages [19], [20] and magnetic microrobots [21] were developed for cell orientation control; however, these methods require additional hardware and alter the standard setup in clinics and biomedical laboratories. The robotic rotation of sperm with a clinically standard setup using a glass micropipette has not been achieved.

Since sperm has a linear shape, the robotic manipulation of sperm is intrinsically a task of manipulating deformable linear objects. The robotic manipulation of macroscale linear objects, such as ropes and cables, is performed with the object's two end points firmly gripped [1], [2]. However, in sperm manipulation, the micropipette allows for its relative movement with the sperm. Path planning methods are lacking for the manipulation under unfixed constraints.

The manipulation of deformable objects also needs to take the object's mechanical properties into account. Mechanical parameters are usually obtained from prior knowledge or characterization. With unknown properties, force sensing is used in deformable object manipulation for hybrid force/position control [22] or impedance control [23]. However, in sperm manipulation, the tail stiffness varies along the tail of a sperm tail and among different sperm. It is time consuming to perform mechanical characterization [24] and difficult to integrate micro–nano force sensors into standard setups in clinical and biomedical laboratories. The unknown and varied mechanical parameters of sperm tail pose difficulties for the robotic manipulation of sperm tail. Finally, the operation time needs to be minimized to maintain a sperm's fertilization capability, which demands the finding of the shortest manipulation path.

This article reports the robotic manipulation of deformable cells with a linear shape. The manipulation of human sperm in clinical cell surgery is used as an example. Since visual feedback of sperm tail is hampered by its low contrast and variations in shape and dimension, deep neural networks were used for robust tail detection, with the issue of data imbalance taken into account. Distinct challenges in cell manipulation that were overcome in this article include the following: 1) limited DOF and unfixed constraints of the micromanipulator on the sperm; 2) variations of tail stiffness along sperm tail and among different sperm; and 3) minimization of operation time to maintain a sperm's fertilization capability. We tackled these challenges by developing a path planning strategy based on manipulation point update, a state transition to determine robot motion based on the configuration of the deformable object, and a model-predictive controller to optimize the manipulation path. Experimental results showed that the orientation error, tail curvedness, and operation time of robotic sperm rotation were all significantly less than those of the manual operation. The lower orientation error and tail curvedness after robotic rotation also led to a higher success rate of subsequent sperm aspiration.

## II. System Setup

As shown in Fig. 2(a), the system consists of an inverted microscope equipped with an $XY$ motorized stage (H117, Prior) and two four-DOF micromanipulators (MX7600, Siskiyou, Grants Pass, OR, USA). The motorized stage is used to position the sperm in the $XY$ plane. A standard injection micropipette (MIC-50-35, Origio, Måløv, Denmark) mounted on the micromanipulator is used for robotic cell manipulation. A hydraulic pump (CellTram, Eppendorf, Hamburg, Germany) is connected with the micropipette for sperm aspiration. A camera (scA1300-32gm, Basler, Ahrensburg, Germany) connected to the microscope captures images at 30 frames/s for tail detection and visual feedback of tail manipulation.

The work flow of robotic sperm manipulation is summarized in Fig. 2(b). A user selects a target sperm via computer mouse clicking. The sperm is immobilized, after which its tail is perpendicular to the micropipette. Since the tail is not coaxial with the micropipette, it would take a high flow rate to aspirate the sperm, risking the loss of the sperm when it quickly enters the

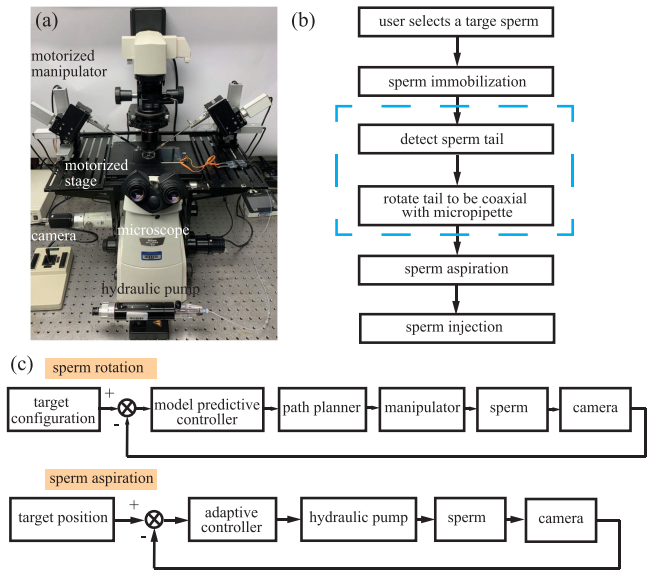


Fig. 2. (a) System setup. (b) Work flow of robotic sperm manipulation. A target sperm is selected by the user and robotically immobilized, after which the tail orientation of the immobilized sperm is perpendicular to the micropipette, not suitable for sperm aspiration. To rotate the sperm tail, the sperm tail is detected by deep neural networks for visual feedback. Then, the micropipette is controlled to rotate the tail to be coaxial with the micropipette. The sperm is then aspirated into the micropipette for further steps in clinical cell surgery. This article is focused on sperm tail detection and robotic sperm rotation control, within the dashed rectangle. (c) Control diagrams of sperm rotation and aspiration. To robotically rotate a sperm, with visual feedback, the developed model-predictive controller and path planner generate robot motion for sperm manipulation. To precisely aspirate sperm and position it within micropipette, a model-based adaptive controller [25] was developed to control piston motion of the hydraulic pump, based on the visual feedback of sperm position.

micropipette under the high flow rate. To rotate the sperm tail, the sperm tail is detected by deep neural networks for visual feedback. Then, the micropipette is controlled to rotate the tail to be coaxial with the micropipette. The sperm is then aspirated into the micropipette for further steps in clinical cell surgery. The cell manipulation tasks on which this article is focused are enclosed by the dashed rectangle in Fig. 2(b).

## III. Sperm Tail Detection

Sperm tail detection is required to provide visual feedback for robotic manipulation. A sperm tail has a length of 50 $\mu$m and a diameter less than 1 $\mu$m and is low in contrast under microscopy, as shown in Fig. 3. Several techniques have been developed for sperm tail segmentation. A Kalman filter was integrated into a maximum intensity region algorithm to detect the sperm tail [26]. The structural similarity index was used to trace the sperm tail in an iterative manner [27]. Fuzzy C means clustering was used to segment the sperm and further divide it into head and tail [28]. However, these methods rely on prior knowledge of sperm tail, such as shape and dimension, and cannot accommodate the variance of tails among different sperm in terms of shape, length, and width [see Fig. 3(a) and (b)]. Moreover, for an immobilized sperm, its tapped point is attached to the substrate, while the other parts are a few micrometers above the substrate [see Fig. 1(f)]. Due to the limited depth of field under microscopy, these parts exhibit different focus and image intensity [see Fig. 3(b)], and the out-of-focus parts can be incorrectly segmented as the background.

To overcome these issues, we developed deep neural networks with robustness to tail variances. Compared to conventional image processing techniques, neural networks can learn features from raw images [29], [30]. We used U-Net as the network architecture for its effectiveness in image segmentation [31], [32]. It is composed of a contracting path and an expansive path, forming a U-shape structure [see Fig. 3(e)]. The left contracting path includes repeated application of two convolution layers, each followed by a max pooling layer for downsampling. After each downsampling operation, the resolution of a feature map decreases by half and the number of feature channels doubles, with the channel numbers labeled under each layer in Fig. 3(e). This endows the network with robustness to noise and translation invariance. In the right expansive path, each upconvolution (upsampling and convolution) layer halves the number of feature channels and, then, concatenates with the feature map at corresponding resolution in the extracting path. Each upconvolution layer is followed by two convolution layers, and the last convolution layer of the networks has two feature channels, corresponding to the two classes of tail and nontail in classification.

Intrinsically, the segmentation of sperm tail is the classification of image pixels into two classes of tail and nontail. In tail detection, data imbalance between the two classes must be dealt with, i.e., the pixels of tail (positive) are much fewer than those of nontail (negative). This imbalance causes the trained networks to be biased toward nontail due to the high true negative rate. To solve this problem, the dice coefficient is used as the loss function in U-Net training instead of the commonly used cross entropy. The dice coefficient is similar to cross entropy by quantifying the difference between the ground truth and classification results [33], but does not count the true negatives. It is expressed as

$$\text{Dice} = \frac{2\text{TP}}{2\text{TP} + \text{FP} + \text{FN}} \tag{1}$$

where TP, FP, and FN are true positives, false positives, and false negatives, respectively.

The sperm tails are manually labeled as ground truth, by drawing a curve along the sperm tail [see the dashed curve in Fig. 3(c)]. To include features such as tail width and intensity transition between the tail and surrounding background in network training, especially for those parts that are out of focus, the pixels around the sperm tail are also labeled as tail. This also increases the number of pixels belonging to the class of tail and helps reduce the bias caused by the data imbalance. Using the trained neural networks, the contour of the detected sperm tail is shown in Fig. 3(d).

## IV. Robotic Sperm Manipulation

### A. Problem Formulation

Sperm tail detection by the neural networks is used to provide visual feedback for robotic manipulation. The manipulation task

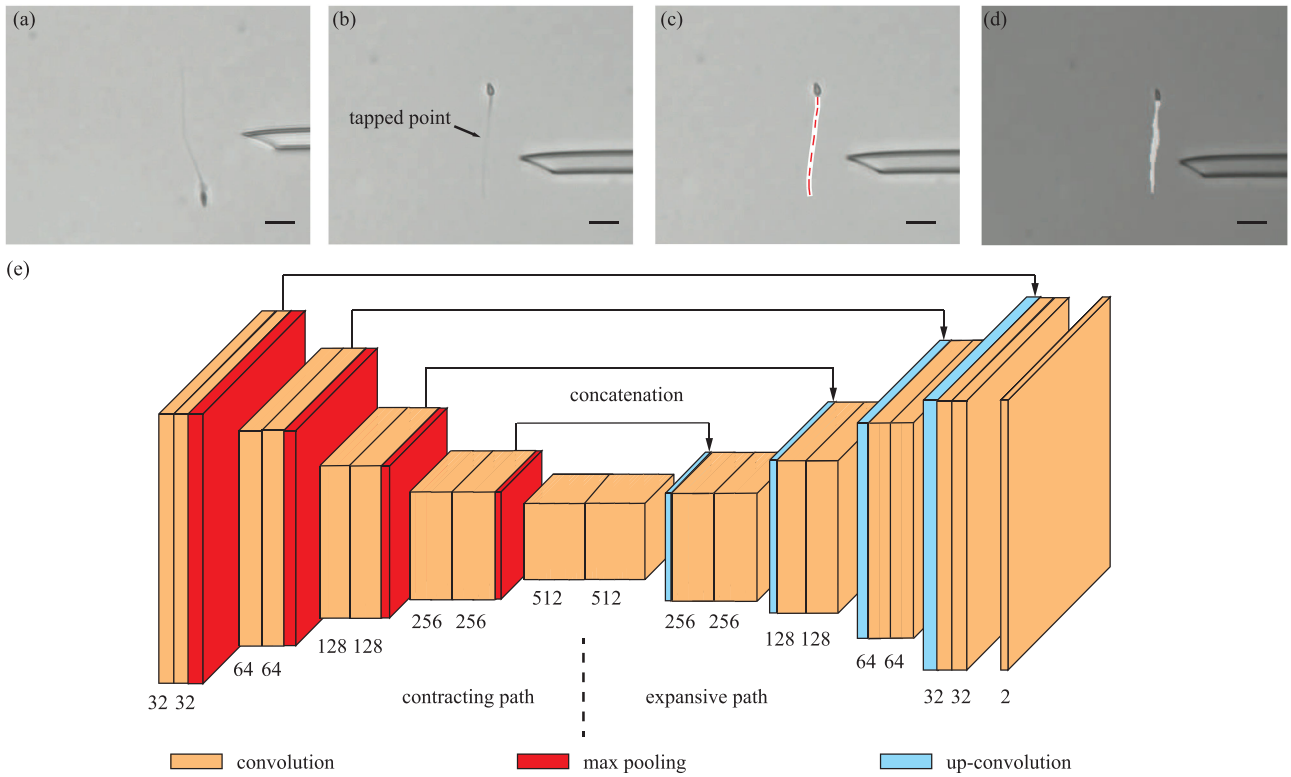


Fig. 3. (a) and (b) Tails of different sperm vary in shape, length, and width. For a sperm after immobilization (b), its tapped point is attached to the substrate, while the other parts are a few micrometers above the substrate, causing focus variance along the tail. (c) Sperm tail is manually labeled as ground truth by drawing a curve along the sperm tail, as indicated by the dashed curve. To include features such as tail width and intensity transition between the tail and surrounding background, the pixels around the sperm tail are also labeled as tail. This also helps reduce the bias caused by the data imbalance. (d) Using the trained neural networks, the contour of the sperm tail is detected. (e) Architecture of the developed neural networks is based on U-Net, with a contracting path and an expansive path. The left contracting path includes repeated application of two convolution layers, each followed by a max pooling layer for downsampling. The right expansive path contains multiple upconvolution (upsampling and convolution) layers, each followed by two convolution layers. Scale bar: 10 $\mu$m.

is to rotate the sperm tail to be coaxial with the micropipette and minimize the tail curvedness. Robotic sperm manipulation is intrinsically deformable linear object manipulation. The robotic manipulation of deformable linear objects needs to take their deformation into account. Various models were developed to describe an object's deformation behavior. Elastic models of a deformable linear object were established based on local deformation and the object's material's Young's modulus and Poisson's ratio [34]. In finite-element models, strain energy was quantified for each element, and the object's stiffness matrix was determined from the total strain energy and displacement vector [35]. Mechanical parameters in these models can be attained from prior knowledge [36] or estimated by characterization [37]. However, for biological cells, their mechanical properties vary significantly, and the characterization process is time consuming [24]. For instance, it takes 5 min to measure a cell's Young's modulus using micropipette aspiration [38]. With unknown mechanical properties of a deformable object, force sensors were used to provide feedback for the control of grasping force [39]. Owing to integration difficulties (e.g., gluing and meticulous alignment) at microscale, force sensors are difficult to integrate into standard setups in clinical and biomedical labs, which utilize glass micropipettes and pure visual feedback for cell manipulation. Thus, cell manipulation involves large model uncertainty, due to cell's unknown and varied mechanical parameters.

Path planning for the manipulation of a deformable object has been extensively studied. A randomized algorithm was proposed to compute the manipulation path that minimizes an energy function based on the object's elasticity [34]. The algorithm focused on the motion of the deformable object, but did not plan the manipulator's motion. Probabilistic roadmap methods were developed to determine the motion of deformable linear objects [1], [4], based on which inverse kinematics was used to derive the corresponding robot motion. For deformable linear objects with environment contacts, two-stage planning was designed to first reach an initial pose for making contact and then use the contact to achieve target configuration [40]. A learning-based approach was also developed by using human demonstration to generate a feasible robot trajectory to manipulate deformable linear objects [41]. These path planning methods were based on the assumption of fixed constraints, i.e., the linear object's two end points were firmly grasped. However, in cell manipulation, the constraints by the micropipette on the cell are unfixed, i.e., there is relative movement between the micropipette and the cell. Methods are lacking for path planning under unfixed constraints to manipulate deformable objects.

Moreover, different from the two grippers used in the manipulation of ropes, wires, and so on, a micropipette is used as a single-ended end-effector in the manipulation of cells. Typical micromanipulators only have translational DOFs and lack rotational DOFs since rotation-induced translation easily

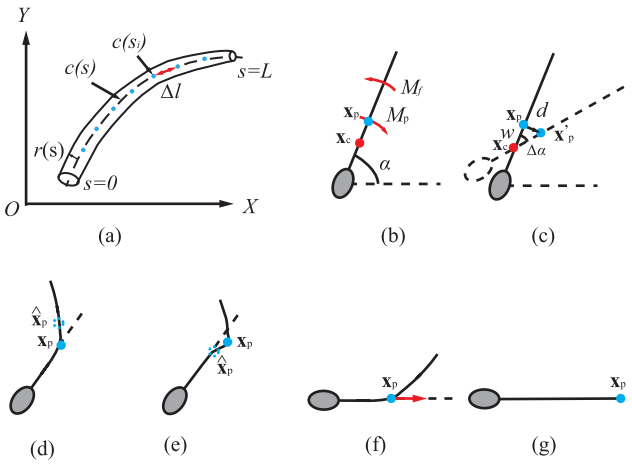


Fig. 4. (a) Geometric model of the deformable linear object. (b) Kinematic model of sperm rotation. The micropipette pushes the sperm tail at $\mathbf{x}_p$ above the mass center $\mathbf{x}_c$, providing a clockwise moment $M_p$. The sperm also encounters a friction moment $M_f$ by the surrounding fluid in culture medium. (c) In a rotation step, the sperm tail is pushed for a distance $d$ by the micropipette, and the corresponding rotation angle $\Delta\alpha$ and next manipulation point after pushing $\mathbf{x}'_p$ can be determined. (d) Path planning algorithm updates the manipulation point $\hat{\mathbf{x}}_p$ to reduce the bending of sperm tail under the fluid friction. (e) Manipulation point is updated to handle the variance of tail stiffness when the tail is deformed under micropipette pushing, but the sperm is not rotated. (f) Tail end remains bent because its stiffness is insufficient to be manipulated for rotation. (g) To minimize the curvedness of the sperm tail, the micropipette is controlled to push along the $X$-axis. Because of the low stiffness of the tail end, the sperm is pushed to be straight without altering its position and orientation.

moves the end-effector out of the limited field of view and focus under a microscope [42]. Therefore, it is challenging to control infinitive DOFs of a deformable object, such as the sperm tail, by a micropipette with limited DOFs.

### B. Geometric Modeling

To describe the deformation of a sperm tail, a geometric model is established to represent the deformable linear object, as shown in Fig. 4(a). The curved cylinder has a length of $L$ and a varied radius of $r(s)$. The axis of this cylinder is a curve $l$ and is parameterized in the Cartesian coordinate frame as

$$l(s) \in \mathbf{R}^2, \text{with } s \in [0, L]. \tag{2}$$

For a sperm, $l(0)$ is the sperm head and $l(L)$ is the end of the sperm tail. The radius $r$ of the sperm tail decreases from the sperm head to the tail end.

To quantify the curvedness of the sperm tail, the curve $l(s)$ is further discretized into multiple control points. The control points are used for determining tail curvedness and the candidates for manipulation point in path planning. For each control point $l(s_i)$, its curvature $c(s_i)$ is calculated from the point and its two neighboring points $l(s_{i-1}), l(s_{i+1})$. A quadratic curve is fit on these three points as

$$\begin{aligned} x &= a_1 + a_2 t + a_3 t^2 \\ y &= b_1 + b_2 t + b_3 t^2. \end{aligned} \tag{3}$$

The six unknown parameters $a_1, a_2, a_3, b_1, b_2$, and $b_3$ can be solved from the coordinates of the three points in the $O$–$XY$ coordinate system. The curvature $c$ is then

$$c = \frac{x''y' - x'y''}{[(x')^2 + (y')^2]^{\frac{3}{2}}} = \frac{2(a_3 b_2 - a_2 b_3)}{(a_2^2 + b_2^2)^{\frac{3}{2}}}. \tag{4}$$

A configuration of the deformable linear object is defined as $q = (l, c)$. The curvedness $C$ of the curve $l$ is defined as

$$C = \sum_i c(s_i). \tag{5}$$

*Remark 1:* The deformable object is modeled in a 2-D space here because the manipulated sperm has a low height of only a few micrometers and is on a substrate (i.e., Petri dish bottom). The geometric model can be readily expanded to 3-D for modeling other deformable linear objects.

### C. Kinematic Modeling

A kinematic model is further developed to describe the sperm rotation process. In Fig. 4(b), a sperm's tail has an orientation error $\alpha$, and it needs to be clockwise rotated to reduce the orientation error. The mass center $\mathbf{x}_c(x_c, y_c)$ of the sperm is

$$\begin{aligned} x_c &= \sum_x \sum_y x\rho(x,y) / \sum_x \sum_y \rho(x,y) \\ y_c &= \sum_x \sum_y y\rho(x,y) / \sum_x \sum_y \rho(x,y) \end{aligned} \tag{6}$$

where $(x, y)$ are all the points within the sperm contour, including the head and detected tail, and $\rho$ is the density of the sperm.

To provide a clockwise moment $M_p$ to rotate the sperm tail, a micropipette is controlled to push the sperm tail at the manipulation point $\mathbf{x}_p$, which is above $\mathbf{x}_c$. The sperm is in culture medium, and it encounters a friction moment $M_f$ by the fluid during rotation. Since the micropipette moves at a constant speed, quasi-static dynamics is assumed, and the driving moment is balanced by the friction moment.

To determine the manipulation point in each rotation step, assume in one step that the manipulation point $\mathbf{x}_p$ has a distance $w$ from the sperm mass center $\mathbf{x}_c$, as shown in Fig. 4(c). Micropipette pushing is perpendicular to the sperm tail with a distance $d$. The corresponding rotation angle of the sperm tail is determined as $\Delta\alpha = \arctan\frac{d}{w}$. The manipulation point after pushing, $\mathbf{x}'_p(x'_p, y'_p)$, is expressed as

$$\begin{aligned} x'_p &= x_p + d\sin\alpha \\ y'_p &= y_p - d\cos\alpha. \end{aligned} \tag{7}$$

### D. Path Planning

To rotate the object, the manipulation path can be derived by connecting the manipulation point in (7) of each rotation step. However, since the sperm tail is highly deformable, this approach only manipulates a small part of the sperm tail, while the remaining part bends under the friction from the surrounding fluid [see Fig. 4(d)]. To control the deformation along the sperm tail, the manipulation point is updated in each rotation step. The change of the manipulation point is applicable in standard clinical setups because the constraints of the micropipette on

**Algorithm 1:** Path Planning With the State Transition Function.

**Input** desired configuration $q_d$, current configuration $q$, pushing distance $d$
**Output** coordinate of manipulation point

Compute mass center $x_c$ by (6)
initial manipulation point $\mathbf{x}_p^0$ determined from $x_c$
**while** orientation error $\alpha > \gamma$ **do**
  $d \leftarrow$ controller (12)–(16)
  $\mathbf{x}_p^n$ determined from $d$ by (7)
  $\hat{\mathbf{x}}_p^n \leftarrow$ STATE TRANSITION ($q_d$, $q$)
**end while**
**function** state transition $q_d$, $q$
  **for** $i = 0, \ldots, N$ **do** ▷ search among control points
    **if** $c(s_i) > \delta$ and $c(s_{i-1}) > \delta$ and $c(s_{i+1}) > \delta$ **then**
      $\hat{\mathbf{x}}_p \leftarrow l(s_i)$
      **break**
    **end if** ▷ overcome tail bending under friction
    **if** $c(s_i) < 0$ and $|c(s_{i-1})| < \delta$ **then**
      $\hat{\mathbf{x}}_p \leftarrow l(s_i)$
      **break**
    **end if** ▷ handle variance of tail stiffness
  **end for**
**end Function**

sperm are unfixed and allow for relative movement between the micropipette and the sperm. Path planning is based on the tail's deformation behavior, with its geometrical model established in Section IV-A. A configuration $q$ of the sperm tail is represented by its centerline curve $l$ and curvature $c$ along the curve. After each rotation step, the current configuration of the sperm tail is obtained by visual feedback. A state transition function $f$ is defined to determine the updated manipulation point $\hat{\mathbf{x}}_p$ based on the current configuration $q$ and the target configuration $q_d$

$$\hat{\mathbf{x}}_p = f(q, q_d). \tag{8}$$

To reduce the bending of sperm tail under fluid friction, the state transition function searches among control points $l(s_i)$ to determine the updated manipulation point. It starts from the first control point and toward the tail end $l(L)$ to find the first control point with its own and two neighboring control points' curvatures all higher than a threshold $\delta$ [see the dashed circle in Fig. 4(d)]. The manipulation point in this rotation cycle is updated to be the control point $\hat{\mathbf{x}}_p$ to reduce the curvature around this region, as shown in Fig. 4(d).

*Remark 2:* Path planning is designed for the manipulation of a deformable linear object when the manipulator's DOF is limited. It is achieved by changing the manipulation point according to the object's deformation behavior, under the unfixed constraints between the manipulator and the object. The method is suitable for micromanipulation, where unfixed constraints are typical, and can be generalized to the manipulation of macroscale deformable objects.

Another challenge in sperm manipulation is the stiffness variance along the sperm tail. As shown in Fig. 1(a), the diameter of a sperm tail decreases from head to end, causing a reduction of stiffness along the tail. The manipulation point is updated toward the tail end, and after several rotation cycles, the micropipette reaches a point with low stiffness. At this point, the tail is deformed under micropipette pushing, but the sperm is not rotated [see Fig. 4(e)]. The state transition function then locates the control point whose curvature is negative and its neighboring control point whose curvature is less than the threshold $\delta$. This point is where the tail bends in the direction of micropipette pushing, but the tail before this point remains straight without being rotated [see the dashed circle in Fig. 4(e)]. It is selected as the updated manipulation point.

After the update in Fig. 4(e), the update of the manipulation point stops since the remaining tail has insufficient stiffness to be manipulated for rotation. This causes the remaining sperm tail to bend due to fluid friction even when the tail before the manipulation point is rotated to the target orientation with orientation error $\alpha < \gamma$ [see Fig. 4(e)]. To minimize the curvedness of the whole sperm tail, the micropipette is controlled to push along the $X$-axis, as indicated by the arrow in Fig. 4(f). Because of the low stiffness of the remaining part of the sperm tail, the remaining part is pushed to be straight without altering the sperm's position and orientation [see Fig. 4(g)].

*Remark 3:* The manipulation of deformable objects must take the object's mechanical parameters into account. Since it is difficult to characterize each point of the deformable object with varied mechanical parameters, the manipulation path is updated based on the object's deformation behavior to handle the stiffness variance, without performing mechanical characterization. This general strategy can be applied to the manipulation of deformable objects with unknown and varied mechanical parameters.

The implementation of the path planning strategy to rotate the sperm tail is shown in Algorithm 1. The initial manipulation point $\mathbf{x}_p^0$ is determined based on the mass center $\mathbf{x}_c$ in (6). For instance, to clockwise rotate the sperm in Fig. 4(b), $\mathbf{x}_p^0$ should be above $\mathbf{x}_c$ on the sperm tail. It also helps prevent the micropipette contact the sperm head to avoid damaging the head-contained genetic materials.

The control diagram is shown in Fig. 5, where the orientation error $\alpha$ is the difference between the desired orientation $\theta_d$ and the current orientation $\theta$ from visual feedback. The controller designed in the following section outputs the pushing distance $d$ of the micropipette. The path planner then determines the manipulation point, i.e., micropipette position, and the manipulator moves accordingly. This control loop is commonly found in the manipulation of rigid objects [43], [44]. To manipulate a deformable object, an additional state transition function is incorporated (highlighted box in Fig. 5). As the rotation steps proceed, the state transition function takes the target configuration and the current configuration from visual feedback as input and updates the manipulation point along the sperm tail in order to minimize the tail curvedness and handle the stiffness variance along the tail.

### *E. Controller Design*

The control task is to rotate the sperm tail to the target orientation, i.e., to be coaxial with the micropipette. Moreover,

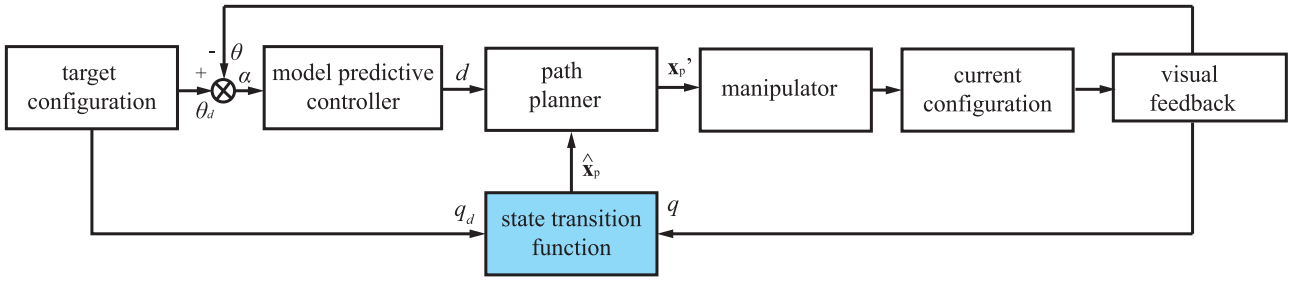


Fig. 5. Control diagram. The orientation error $\alpha$ is the difference between the desired orientation $\theta_d$ and the current orientation $\theta$ from visual feedback. The model-predictive controller outputs the pushing distance $d$ of the micropipette. The cost function of the control is designed to minimize the orientation error and the manipulation path length. The path planner then determines the manipulation point (micropipette position), and the manipulator moves accordingly. To manipulate a deformable object, an additional state transition function is incorporated. As the rotation steps proceed, the state transition function takes the target configuration and the current configuration from visual feedback as input and updates the manipulation point along the sperm tail in order to reduce the tail curvedness and handle the stiffness variance of the tail.

the time of sperm rotation needs to be minimized to maintain the sperm's fertilization potential. The minimization of time corresponds to finding the shortest manipulation path. Thus, a model-predictive controller is designed. It is an approach of optimal control, which iteratively performs optimization over a finite period of time instead of finding a global minimum [45]. As the manipulation path length is related to the manipulation point in each control cycle, the model-predictive controller performs optimization after each manipulation point update. In contrast, a linear–quadratic regulator (LQR) optimizes over the entire control process [46] and cannot dynamically optimize along with the manipulation point change.

The dynamics of sperm rotation is

$$I\ddot{\theta} + D\dot{\theta} = M_p - M_f \tag{9}$$

where $I$ and $D$ are inertial and damping coefficients, respectively, and $M_p$ and $M_f$ are moments from the pushing micropipette and the fluid friction, respectively.

The state space of the model (9) in discrete time is

$$\mathbf{x}(k+1) = \mathbf{A}\mathbf{x}(k) + \mathbf{B}u(k) \tag{10}$$

where

$$\mathbf{x} = \begin{bmatrix} \theta \\ \dot{\theta} \end{bmatrix}, \mathbf{A} = \begin{bmatrix} 0 & 1 \\ 0 & -\frac{D}{I} \end{bmatrix}, \mathbf{B} = \begin{bmatrix} 0 \\ \frac{1}{I} \end{bmatrix}. \tag{11}$$

The control input $u$ here in each control cycle is the pushing distance $d$ of the micropipette. The sum of the pushing distance is the length of the manipulation path.

The model-predictive controller predicts the model state $\mathbf{X}_k$ and control input $\mathbf{U}_k$ in the next $p$ control cycles as

$$\mathbf{X}_k = [\mathbf{x}(k+1|k)^T\ \mathbf{x}(k+2|k)^T \dots \mathbf{x}(k+p|k)^T]^T \tag{12}$$

$$\mathbf{U}_k = [\mathbf{u}(k|k)^T\ \mathbf{u}(k+1|k)^T \dots \mathbf{u}(k+p-1|k)^T]^T. \tag{13}$$

From (10), (12), and (13), we can obtain

$$\mathbf{X}_k = \Psi\mathbf{x}(k) + \Theta\mathbf{U}_k \tag{14}$$

where

$$\Psi = \begin{bmatrix} \mathbf{A} \\ \mathbf{A}^2 \\ \vdots \\ \mathbf{A}^p \end{bmatrix}, \Theta = \begin{bmatrix} \mathbf{B} & \mathbf{0} & \cdots & \mathbf{0} \\ \mathbf{AB} & \mathbf{B} & \cdots & \mathbf{0} \\ \vdots & \vdots & \ddots & \vdots \\ \mathbf{A}^{p-1}\mathbf{B} & \mathbf{A}^{p-2}\mathbf{B} & \cdots & \mathbf{B} \end{bmatrix}. \tag{15}$$

The cost function $J(\mathbf{U}_k)$ for the optimization of the manipulation path is formulated as

$$J(\mathbf{U}_k) = (\mathbf{X}_k - \mathbf{D}_k)^T\mathbf{W}_1(\mathbf{X}_k - \mathbf{D}_k) + \mathbf{U}_k^T\mathbf{W}_2\mathbf{U}_k \tag{16}$$

where $\mathbf{W}_1$ and $\mathbf{W}_2$ are the weights for the orientation error and the length of manipulation path, respectively.

In sperm rotation, the control input $u$ needs to be constrained since too large pushing distance of the micropipette can cause sperm translation and move the rotation center. As shown in Fig. 4(c), a large pushing distance leads to a small angle between micropipette motion and sperm tail and causes a large part of micropipette motion to be along the sperm tail and move the sperm. The constraints are expressed as $0 < \mathbf{U}_k < \Gamma$, with $\Gamma$ containing $p$ elements of $\gamma$ as the constraints for the next $p$ control cycles.

The control input can be solved from the cost function with quadratic programming [47], and its first element is the control input in the current control cycle. The pushing distance $d$ of the micropipette is determined by the controller and forwarded to the path planner, as shown in Fig. 5.

*Remark 4:* The model-predictive controller designed here provides a general form of control for manipulation with optimization objectives. In this article, the cost function incorporates the orientation error and the manipulation path length. Metrics, such as the object's deformation and strain, can also be integrated into the cost function in other applications.

## V. Results and Discussion

Human sperm used in the experiments were obtained from the CReATe Fertility Centre, Toronto, ON, Canada. Approval was obtained from the Research Ethics Board of the University of Toronto (application number UT35544). Informed consent was obtained from all subjects. The standard clinical setup was used,

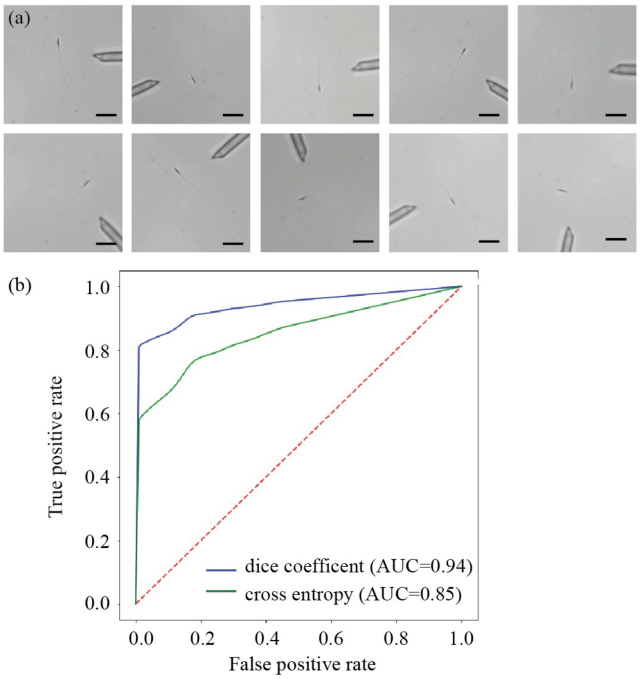


Fig. 6. (a) Images augmented from a single sperm image by applying a combination of transformations, such as flipping, rotation, random brightness, and contrast adjustment. (b) ROC curves of the developed neural network. The networks with the dice coefficient as a loss function achieved an AUC of 0.94 versus 0.85 by using cross entropy as a loss function. Scale bar: 10 $\mu$m.

where the micromanipulator had only translational DOFs, and an injection micropipette was used for sperm manipulation.

### A. *Sperm Tail Detection Results*

To manipulate a sperm tail, tail detection is required to provide visual feedback. For an immobilized sperm, its tapped point is attached to the substrate, while the other parts are a few micrometers above the substrate, causing focus variance along the tail [see Fig. 3(a) and (b)]. To prepare the dataset for training the deep neural networks, we collected microscopy images of 200 sperm after they were immobilized. The dataset was further augmented by applying a combination of transformations, such as flipping, rotation, random brightness, and contrast adjustment. Ten images augmented from a single sperm image are shown in Fig. 6(a). The augmentation step helped increase the dataset size to 2000.

Data imbalance in the dataset, i.e., the pixels of tail (positive) are much fewer than those of nontail (negative), causes the trained networks to be biased toward nontail due to the high true negative rate. Thus, the dice coefficient in (1) was used as the loss function rather than the commonly used cross entropy for network training. The dice coefficient does not count the true negatives; thus, the networks were forced to learn more on the sperm tail. Besides the manually labeled curve along the sperm tail, the pixels around the sperm tail were also labeled as tail to include features such as tail width and intensity transition around the tail, as shown in Fig. 3(c).

TABLE I
PERFORMANCE OF SPERM TAIL DETECTION BY DEEP NEURAL NETWORKS AND THRESHOLDING

| | | Performance(%) | | |
|---|---|---|---|---|
| | | Neural networks | | Thresholding |
| Metric | Definition | Cross entropy | Dice coefficient | |
| Accuracy | $\frac{TP+TN}{Sum}$ | 95 | 98 | 81 |
| Precision | $\frac{TP}{TP+FP}$ | 84 | 96 | 67 |
| Sensitivity | $\frac{TP}{TP+FN}$ | 85 | 94 | 70 |
| Specificity | $\frac{TN}{FP+TN}$ | 96 | 99 | 86 |
| Dice coefficent | $\frac{2TP}{2TP+FP+FN}$ | 87 | 94 | 69 |

TP: true positive, TN: true negative, FP: false positive, and FN: false negative.

The dataset was separated into 80% for training, 10% for validation, and 10% for test. The trained networks achieved an accuracy of 99% for sperm tail detection in the test set. To further evaluate the performance of the developed neural networks, additional 200 sperm images were captured for test. The test results were used to plot receiver operating characteristics (ROC) curve for assessing classifiers [48]. As shown in Fig. 6(b), the ROC curve plots true positive rate versus false positive rate. The area under curve (AUC) for the networks with the dice coefficient as the loss function was 0.94 outperformed the AUC of 0.85 for the networks with cross entropy as the loss function since the dice coefficient alleviated data imbalance by not counting true negatives. As summarized in Table I, the networks achieved 98% in accuracy, 96% in precision, 94% in sensitivity, 99% in specificity, and 94% in dice coefficient, all higher than those by the networks with cross entropy as the loss function. Detection errors occurred when occasionally a sperm tail was attached with cytoplasmic droplet, a form of morphology abnormality [49].

The performance of deep neural networks for sperm tail detection was also compared with traditional image processing. Here, for comparison, we used maximum entropy thresholding [50] to detect the sperm tail. The threshold was determined by maximizing interclass entropy. As summarized in Table I, the thresholding method achieved 81% in accuracy, 67% in precision, 70% in sensitivity, 86% in specificity, and 69% in dice coefficient, all lower than those by the deep neural networks. This is because traditional image processing relies on manually selected features and fails to accommodate sperm variances, while deep neural networks can learn features automatically from raw images [29], [30]. By training on a dataset containing different sperm, the networks gained robustness to tail variances in shape, dimension, and focus.

The time cost for sperm tail detection was 0.02 s (Intel i7 processor, Nvidia GTX1080 GPU). A sperm was tracked by the probabilistic data association filter [20]. A region of interest was then determined for sperm tail, and deep-learning-based tail detection was only performed on this region rather than the whole image to save computation cost.

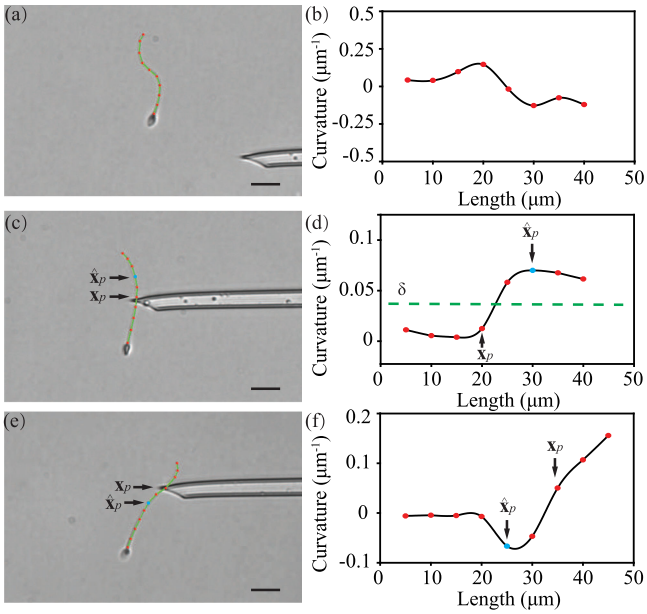


Fig. 7. (a) Configuration $q$ of a sperm tail is composed of a curve $l$ (dashed line) and the curvature $c$ along the curve. The curve is discretized into multiple control points for deformation control. (b) Corresponding curvature for the control points along the sperm tail. (c) Sperm tail after the manipulation point $\mathbf{x}_p$ was bent under fluid friction. (d) State transition function $f$ was formulated to determine the updated manipulation point $\hat{\mathbf{x}}_p$, by locating the control point with its own and two neighboring control points' curvatures all higher than a threshold $\delta$. (e) Micropipette reached a point with low stiffness where the tail was deformed under micropipette pushing, but the sperm was not rotated. (f) State transition function located the control point with the curvature negative and its neighboring control point' curvature less than the threshold $\delta$ as the updated manipulation point $\hat{\mathbf{x}}_p$. Scale bar: 10 $\mu$m.

### *B. Sperm Manipulation Results*

With the detected sperm tail as visual feedback, robotic sperm manipulation was performed to rotate the sperm tail to be coaxial with the micropipette. A geometric model was established in (2) to describe the deformation of a sperm tail. A configuration $q$ of a sperm tail is composed of a curve $l$ [see Fig. 7(a)] and the curvature $c$ along the curve [see Fig. 7(b)]. Based on the curvature of each control point on the curve calculated from (4), the curvedness $C$ of the sperm in Fig. 7(a) was quantified as 0.67 according to (5).

The manipulation task was to rotate the sperm tail to the target orientation and minimize the tail curvedness. This target configuration $q_d$ facilitated subsequent sperm aspiration by preventing a large flow rate to aspirate the sperm. With the kinematic model (7), the manipulation point $\mathbf{x}_p$ in each rotation step was determined. The manipulation path was formed by connecting these points; however, this approach only manipulated a small part of sperm tail, while the remaining part bent under fluid friction [see Fig. 7(c)].

Here, the micropipette, a standard end-effector in clinical cell surgery, imposed only unfixed constraints on the sperm, allowing for relative movement between the micropipette and the sperm. By utilizing the unfixed constraint, a state transition function $f$ was formulated in (8) to determine the updated manipulation point based on target and current configurations (see Algorithm 1). To cope with tail bending under fluid friction shown in Fig. 7(c), the state transition function started from the sperm head to locate the first control point with its own and two neighboring control points' curvatures all higher than a threshold $\delta$ [see Fig. 7(d)]. The corresponding position $\hat{\mathbf{x}}_p$ on the sperm is shown in Fig. 7(c), and the micropipette was controlled to reach this point to reduce the curvature around the point.

The deformation of the sperm tail relates to its mechanical properties. The bending stiffness of human sperm tail was about $4 \times 10^{-21}$ N $\cdot$ m$^2$ [51], but the stiffness varies along the sperm tail and among different sperm [52], causing system uncertainty. While the manipulation point was updated toward the tail end, the micropipette reached a point with low stiffness after several rotation cycles. At this point, the tail was deformed under micropipette pushing, but the sperm was not rotated [see Fig. 7(e)]. In this case, the state transition function located the control point whose curvature was negative and its neighboring control point whose curvature was less than the threshold $\delta$ [see Fig. 7(f)]. This point was where the tail bent in the direction of micropipette pushing, but the tail before this point remained straight without being rotated, as shown in Fig. 7(e). The micropipette was controlled to move to this updated manipulation point $\hat{\mathbf{x}}_p$ to overcome stiffness variance. The process of robotic sperm tail rotation is also shown in the supplementary video.

A model-predictive controller was designed in (14) to predict the model state and control input in the next five control cycles. Based on these predictions, a cost function (16) was formulated to minimize the manipulation path length and the orientation error. The manipulation path length in each rotation step was approximately the orientation angle times the radius. With a rotation radius of about 10 $\mu$m, to make orientation error and manipulation path length play equal roles in the cost function, the weight for the orientation error was set to be 0.09, and the weight for the manipulation path length was set to be 0.91. For a quantitative comparison of the model-predictive controller, the LQR controller, and the proportional–integral–derivative (PID) controller, 150 sperm were rotated after immobilization, 50 by each control strategy. The LQR controller minimized a quadratic cost function incorporating the orientation error and the manipulation path length. However, different from dynamic optimization in model-predictive control, LQR control optimized over the entire control process. The control gains of the PID controller were finely tuned experimentally. A set of PID parameters was used for sperm rotation, with the cost calculated as the sum of the orientation error and the manipulation path length times their respective weights. The PID parameters with the lowest cost were adopted for sperm manipulation. Owing to the time cost of the communication between the computer and the manipulator as well as the robot motion, the time for each control cycle (rotation step) was approximately 0.2 s.

Fig. 8(a) shows the orientation error during sperm rotation by the model-predictive controller, the LQR controller, and the PID controller. In three experiments, the sperm had initial orientation errors around 90°. The model-predictive controller reduced the error to less than 1° within 6 s. In contrast, the PID controller took over 9 s and the LQR controller took about 8 s to reduce the error to less than 1°. The model-predictive controller took less

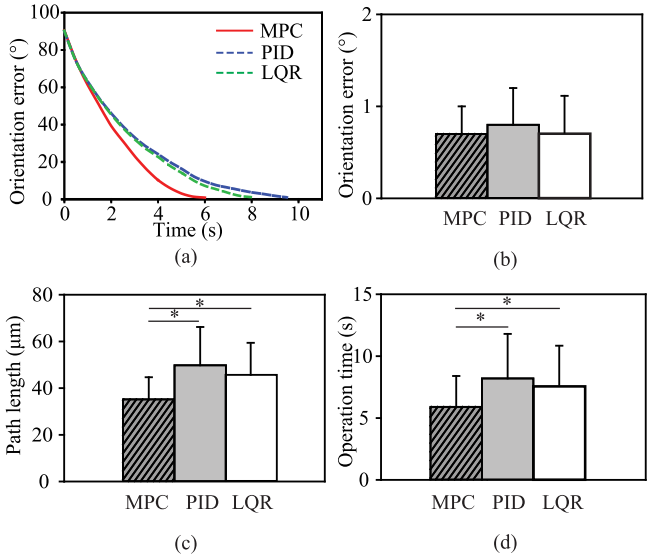


Fig. 8. (a) Orientation error during sperm rotation. The model-predictive controller (MPC) took less time to reach the orientation error $< 1^\circ$ than the PID and LQR controllers. (b) Final orientation error of the model-predictive controller was not significantly different from the error of the PID and LQR controllers. (c) Manipulation path length of the model-predictive controller was significantly less than those of the PID and LQR controllers. (d) Shorter manipulation path led to significantly less operation time of the model-predictive controller than those of the PID and LQR controllers.

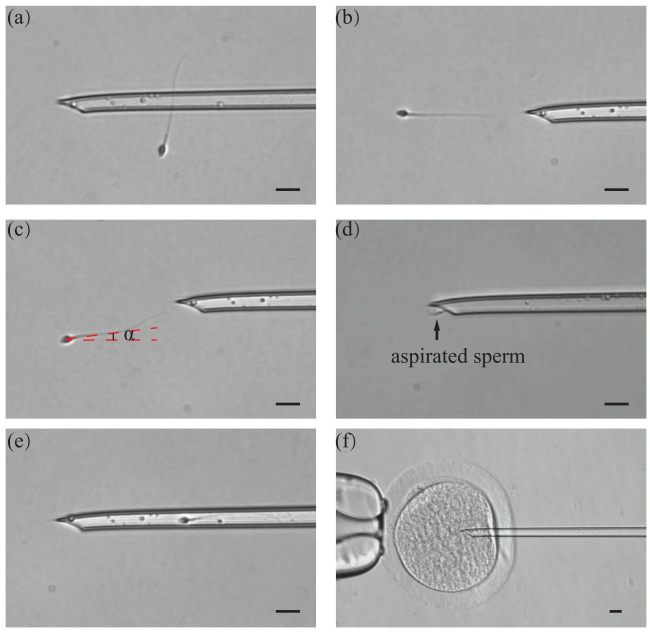


Fig. 9. (a) Sperm was robotically immobilized by tapping its tail with a micropipette. (b) Robotic sperm manipulation was performed to rotate the sperm tail to be coaxial with the micropipette and minimize the tail curvedness. (c) Manual sperm rotation was a trial-and-error process, suffering from large orientation error $\alpha$ and tail curvedness. (d) Sperm after robotic rotation was aspirated into the micropipette at a lower speed, due to less orientation error and tail curvedness. (e) Sperm after robotic rotation was successfully positioned within the micropipette. (f) Sperm was injected into an oocyte for clinical *in vitro* fertilization. Scale bar: 10 $\mu$m.

operation time by dynamically optimizing the manipulation path based on the designed cost function. The results showed that the orientation error of $0.7 \pm 0.3^\circ$ by the model-predictive controller was not significantly different from the errors of $0.8 \pm 0.4^\circ$ by the PID controller and $0.7 \pm 0.4^\circ$ by the LQR controller ($p > 0.05$, $n = 50$ for each control strategy), as shown in Fig. 8(b). However, the manipulation path length of the model-predictive controller was $35.2 \pm 9.5$ $\mu$m, significantly less than those of $49.8 \pm 16.4$ $\mu$m by the PID controller and $45.6 \pm 13.2$ $\mu$m by the LQR controller ($p < 0.05$ and $n = 50$ for each control strategy), as shown in Fig. 8(c). This led to significantly less operation time of $5.9 \pm 2.5$ s by the model-predictive controller than those of $8.2 \pm 3.6$ s by the PID controller and $7.6 \pm 3.1$ s by the LQR controller ($p < 0.05$ and $n = 50$ for each control strategy), as shown in Fig. 8(d).

To further compare the performance of robotic sperm rotation with the manual approach, experiments were performed on another 200 human sperm. After sperm immobilization in Fig. 9(a), 100 sperm were robotically rotated [see Fig. 9(b)] and the other 100 sperm were manually rotated by an experienced operator [see Fig. 9(c)]. The experimental results showed that the orientation error of robotic sperm rotation was $0.8 \pm 0.3^\circ$, significantly less than the error of $4.1 \pm 2.4^\circ$ by manual rotation ($p < 0.05$ and $n = 100$ in each group), as shown in Fig. 10(a). In robotic sperm rotation, the model-predictive controller (14) minimized the orientation error based on visual feedback (see Fig. 5). In contrast, manual rotation was a trial-and-error process by repeatedly pushing the sperm tail with a micropipette.

The curvedness defined in (5) reflects the deformation of the sperm tail and is needed to be minimized before aspiration. Robotic sperm rotation achieved a curvedness of $0.14 \pm 0.04$ $\mu$m$^{-1}$, significantly less than the curvedness of $0.50 \pm 0.21$ $\mu$ m$^{-1}$ by manual rotation ($p < 0.05$ and $n = 100$ in each group), as shown in Fig. 10(b). The results showed that the state transition function in Algorithm 1 was able to effectively reduce the curvedness of the sperm tail, based on the visual feedback of the tail's configuration. As shown in Fig. 10(c), the operation time by robotic rotation was $5.6 \pm 2.1$ s, significantly less than the operation time of $12.2 \pm 4.7$ s by manual rotation ($p < 0.05$ and $n = 100$ in each group).

The purpose of rotating a sperm and minimizing its tail curvedness was to facilitate subsequent sperm aspiration [25] in cell surgery. Therefore, we further performed experiments of sperm aspiration after sperm tail rotation, where success was defined as aspirating the sperm into the micropipette and positioning it within the field of view. When comparing the success rates of sperm aspiration after robotic and manual rotation, it was found that robotic sperm rotation achieved a success rate of 97%, higher than that of 76% by manual rotation. Owing to the lower orientation error and tail curvedness after robotic rotation [see Fig. 9(b)], the sperm was aspirated into the micropipette at a lower speed [see Fig. 9(d)] and successfully positioned within the micropipette and the field of view [see Fig. 9(e)]. In contrast, after manual rotation of a sperm, with its tail not exactly coaxially aligned with the micropipette [see Fig. 9(c)], a higher flow rate was required for aspiration since the flow rate attenuated when deviating from the micropipette axis. This caused the sperm to enter the micropipette at a high speed and

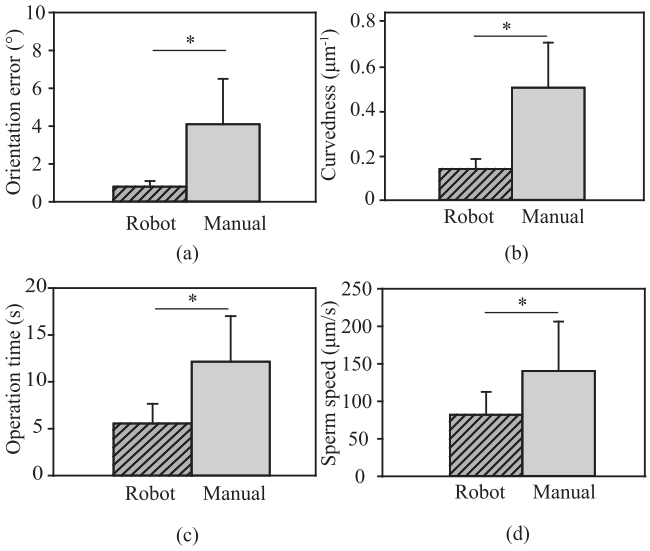


Fig. 10. (a) Orientation error of robotic sperm rotation was significantly less than that by manual rotation. (b) Robotic sperm rotation achieved a curvedness significantly less than that by manual rotation. (c) Operation time by robotic rotation was significantly less than that by manual rotation. (d) Speed of sperm entering the micropipette after robotic sperm rotation was significantly less than that after manual rotation.

increased the chance of losing outside the field of view under microscopy.

To quantitatively compare the speed of sperm entering the micropipette after robotic and manual sperm rotation, sperm tracking [28] was used to calculate the speed based on the sperm positions before and after entering the micropipette and corresponding time instances. As shown in Fig. 10(d), the sperm speed after robotic sperm rotation was $82.1 \pm 30.5$ $\mu$m/s, significantly less than that of $140.4 \pm 65.9$ $\mu$m/s after manual rotation ($p < 0.05$ and $n = 100$ in each group). The corresponding flow rates were derived from the speed of sperm entering the micropipette and micropipette diameter. The flow rate after robotic sperm rotation was $1.61 \pm 0.60$ pL/s, significantly lower than the flow rate of $2.76 \pm 1.29$ pL/s after manual rotation. The higher flow rate after manual rotation increased the likelihood of sperm moving out of the field of view during aspiration. After losing track of the sperm, although the sperm can be slowly pushed back into the field of view by applying positive pressure, it cost additional time for oocyte exposure to ambient environment, negatively impacting the oocyte's development potential [53]. In contrast, robotic sperm rotation greatly facilitated sperm aspiration, after which the sperm well positioned in the micropipette was injected into an oocyte for *in vitro* fertilization [see Fig. 9(f)].

Besides the manipulation of immobilized sperm, the developed methods can also be used for motile sperm manipulation. Before immobilization, a motile sperm is rotated to make its tail vertical to the micropipette such that the tapping micropipette does not touch the sperm head, which contains DNA. In robotic manipulation, to compensate for sperm's intrinsic motion, the $XY$ motorized stage was controlled to keep the target sperm in the center of the field of view (see the supplementary video). The path planning approach and the controller for the manipulator are the same as those in the manipulation of immobilized sperm. Experimental results showed robotic rotation of motile sperm achieved an accuracy of $1.2 \pm 0.4^\circ$, significantly less than the error of $8.9 \pm 5.4^\circ$ by manual rotation ($p < 0.05$ and $n = 100$ in each group). The operation time by robotic rotation of motile sperm was $7.5 \pm 2.1$ s, significantly less than the operation time of $19.1 \pm 10.5$ s by manual rotation ($p < 0.05$ and $n = 100$ motile sperm in each group).

## VI. Conclusion

This article reported the robotic manipulation of deformable cells with a linear shape. To deal with large variance of sperm tails in shape and dimension, deep neural networks were developed for robust tail detection (accuracy: 98%). With the intrinsic challenges in cell manipulation, such as micromanipulator's limited DOFs and cell's varied mechanical parameters, mathematical modeling and path planning strategies were developed to rotate a sperm to the target orientation. A state transition function was formulated to update the manipulation point based on sperm tail's deformation behavior. A model-predictive controller was designed to minimize the orientation error and the manipulation path length. Experiments showed that robotic manipulation achieved an orientation error of $0.8^\circ$, a tail curvedness of 0.025, and an operation time of 5.6 s, all significantly less than those of the manual approach. The superior performance of robotic sperm rotation led to a high success rate of 97% for subsequent sperm aspiration.

## References

[1] M. Saha and P. Isto, "Manipulation planning for deformable linear objects," *IEEE Trans. Robot.*, vol. 23, no. 6, pp. 1141–1150, Dec. 2007.
[2] J. Zhu, B. Navarro, P. Fraisse, A. Crosnier, and A. Cherubini, "Dual-arm robotic manipulation of flexible cables," in *Proc. IEEE/RSJ Int. Conf. Intell. Robots Syst.*, 2018, pp. 479–484.
[3] A. Shademan, R. S. Decker, J. D. Opfermann, S. Leonard, A. Krieger, and P. C. Kim, "Supervised autonomous robotic soft tissue surgery," *Sci. Transl. Med.*, vol. 8, no. 337, 2016, Art. no. 337ra64.
[4] M. Moll and L. E. Kavraki, "Path planning for deformable linear objects," *IEEE Trans. Robot.*, vol. 22, no. 4, pp. 625–636, Aug. 2006.
[5] E. A. Gaffney, H. Gadêlha, D. Smith, J. Blake, and J. C. Kirkman-Brown, "Mammalian sperm motility: Observation and theory," *Annu. Rev. Fluid Mech.*, vol. 43, pp. 501–528, 2011.
[6] S. Johari, V. Nock, M. M. Alkaisi, and W. Wang, "On-chip analysis of C. elegans muscular forces and locomotion patterns in microstructured environments," *Lab Chip*, vol. 13, no. 9, pp. 1699–1707, 2013.
[7] N. Chronis, "Worm chips: Microtools for C. elegans biology," *Lab Chip*, vol. 10, no. 4, pp. 432–437, 2010.
[8] P. Rubino, P. Viganè, A. Luddi, and P. Piomboni, "The ICSI procedure from past to future: A systematic review of the more controversial aspects," *Hum. Reproduction Update*, vol. 22, no. 2, pp. 194–227, 2016.
[9] K. Swann, M. Larman, C. Saunders, and F. Lai, "The cytosolic sperm factor that triggers CA2+ oscillations and egg activation in mammals is a novel phospholipase C: PLC$\zeta$," *Reproduction*, vol. 127, no. 4, pp. 431–439, 2004.
[10] A. Saleh, J. Kashir, A. Thanassoulas, B. Safieh-Garabedian, F. A. Lai, and M. Nomikos, "Essential role of sperm-specific PLC-zeta in egg activation and male factor infertility: An update," *Front. Cell Devlop. Biol.*, vol. 8, p. 28, 2020.
[11] S. Hu and D. Sun, "Automatic transportation of biological cells with a robot-tweezer manipulation system," *Int. J. Robot. Res.*, vol. 30, no. 14, pp. 1681–1694, 2011.
[12] X. Liu, K. Kim, Y. Zhang, and Y. Sun, "Nanonewton force sensing and control in microrobotic cell manipulation," *Int. J. Robot. Res.*, vol. 28, no. 8, pp. 1065–1076, 2009.

[13] S. Permana, E. Grant, G. M. Walker, and J. A. Yoder, "A review of automated microinjection systems for single cells in the embryogenesis stage," *IEEE/ASME Trans. Mechatronics*, vol. 21, no. 5, pp. 2391–2404, Oct. 2016.
[14] C. Leung, Z. Lu, X. P. Zhang, and Y. Sun, "Three-dimensional rotation of mouse embryos," *IEEE Trans. Biomed. Eng.*, vol. 59, no. 4, pp. 1049–1056, Apr. 2012.
[15] M. Hagiwara, T. Kawahara, and F. Arai, "Local streamline generation by mechanical oscillation in a microfluidic chip for noncontact cell manipulations," *Appl. Phys. Lett.*, vol. 101, no. 7, 2012, Art. no. 074102.
[16] H. Shafiee, J. L. Caldwell, M. B. Sano, and R. V. Davalos, "Contactless dielectrophoresis: A new technique for cell manipulation," *Biomed. Microdevices*, vol. 11, no. 5, pp. 997–1006, 2009.
[17] M. Xie, J. K. Mills, Y. Wang, M. Mahmoodi, and D. Sun, "Automated translational and rotational control of biological cells with a robot-aided optical tweezers manipulation system," *IEEE Trans. Autom. Sci. Eng.*, vol. 13, no. 2, pp. 543–551, Apr. 2016.
[18] H. Zhang and K.-K. Liu, "Optical tweezers for single cells," *J. Roy. Soc. Interface*, vol. 5, no. 24, pp. 671–690, 2008.
[19] X. Liu, Z. Lu, and Y. Sun, "Orientation control of biological cells under inverted microscopy," *IEEE/ASME Trans. Mechatronics*, vol. 16, no. 5, pp. 918–924, Oct. 2011.
[20] Z. Zhang *et al.*, "Robotic immobilization of motile sperm for clinical intracytoplasmic sperm injection," *IEEE Trans. Biomed. Eng.*, vol. 66, no. 2, pp. 444–452, Feb. 2019.
[21] M. Hagiwara, T. Kawahara, Y. Yamanishi, T. Masuda, L. Feng, and F. Araib, "On-chip magnetically actuated robot with ultrasonic vibration for single cell manipulations," *Lab Chip*, vol. 11, pp. 2049–2054, 2011.
[22] G. Duchemin, P. Maillet, P. Poignet, and E. Dombre, "A hybrid position/force control approach for identification of deformation models of skin and underlying tissues," *IEEE Trans. Biomed. Eng.*, vol. 52, no. 2, pp. 160–170, Feb. 2005.
[23] Y. Xie *et al.*, "A force control approach to a robot-assisted cell microinjection system," *Int. J. Robot. Res.*, vol. 29, pp. 1222–1232, 2010.
[24] C. Dai *et al.*, "Robotic manipulation of deformable cells for orientation control," *IEEE Trans. Robot.*, vol. 36, no. 1, pp. 271–283, Feb. 2019.
[25] G. Shan, Z. Zhang, C. Dai, X. Wang, L.-T. Chu, and Y. Sun, "Model-based robotic cell aspiration: Tackling nonlinear dynamics and varying cell sizes," *IEEE Robot. Autom. Lett.*, vol. 5, no. 1, pp. 173–178, Jan. 2019.
[26] J. Liu, C. Leung, Z. Lu, and Y. Sun, "Quantitative analysis of locomotive behavior of human sperm head and tail," *IEEE Trans. Biomed. Eng.*, vol. 60, no. 2, pp. 390–396, Feb. 2013.
[27] A. Bijar, A. P. Benavent, M. Mikaeili, and R. Khayati, "Fully automatic identification and discrimination of sperm's parts in microscopic images of stained human semen smear," *J. Biomed. Sci. Eng.*, vol. 5, no. 7, pp. 384–395, 2012.
[28] C. Dai *et al.*, "Automated non-invasive measurement of single sperm's motility and morphology," *IEEE Trans. Med. Imag.*, vol. 37, no. 10, pp. 2257–2265, Oct. 2018.
[29] G. Litjens *et al.*, "A survey on deep learning in medical image analysis," *Med. Image Anal.*, vol. 42, pp. 60–88, 2017.
[30] E. Moen, D. Bannon, T. Kudo, W. Graf, M. Covert, and D. Van Valen, "Deep learning for cellular image analysis," *Nature Methods*, vol. 16, no. 12, pp. 1233–1246, 2019.
[31] T. Falk *et al.*, "U-Net: Deep learning for cell counting, detection, and morphometry," *Nature Methods*, vol. 16, no. 1, pp. 67–70, 2019.
[32] O. Ronneberger, P. Fischer, and T. Brox, "U-Net: Convolutional networks for biomedical image segmentation," in *Proc. Int. Conf. Med. Image Comput. Comput.- Assist. Intervention*, 2015, pp. 234–241.
[33] S. Jha, L. H. Son, R. Kumar, I. Priyadarshini, F. Smarandache, and H. V. Long, "Neutrosophic image segmentation with dice coefficients," *Measurement*, vol. 134, pp. 762–772, 2019.
[34] F. Lamiraux and L. E. Kavraki, "Planning paths for elastic objects under manipulation constraints," *Int. J. Robot. Res.*, vol. 20, no. 3, pp. 188–208, 2001.
[35] H. Lin, F. Guo, F. Wang, and Y.-B. Jia, "Picking up a soft 3D object by 'feeling' the grip," *Int. J. Robot. Res.*, vol. 34, no. 11, pp. 1361–1384, 2015.
[36] J. Smolen and A. Patriciu, "Deformation planning for robotic soft tissue manipulation," in *Proc. IEEE 2nd Int. Conf. Adv. Comput. Hum. Interact.*, 2009, pp. 199–204.
[37] M. Higashimori, K. Yoshimoto, and M. Kaneko, "Active shaping of an unknown rheological object based on deformation decomposition into elasticity and plasticity," in *Proc. IEEE Int. Conf. Robot. Autom.*, 2010, pp. 5120–5126.
[38] M. Khalilian, M. Navidbakhsh, M. R. Valojerdi, M. Chizari, and P. E. Yazdi, "Estimating Young's modulus of zona pellucida by micropipette aspiration in combination with theoretical models of ovum," *J. Roy. Soc. Interface*, vol. 7, no. 45, pp. 687–694, 2010.
[39] A. Delgado, J. A. Corrales, Y. Mezouar, L. Lequievre, C. Jara, and F. Torres, "Tactile control based on Gaussian images and its application in bimanual manipulation of deformable objects," *Robot. Auton. Syst.*, vol. 94, pp. 148–161, 2017.
[40] J. Zhu, B. Navarro, R. Passama, P. Fraisse, A. Crosnier, and A. Cherubini, "Robotic manipulation planning for shaping deformable linear objects with environmental contacts," *IEEE Robot. Autom. Lett.*, vol. 5, no. 1, pp. 16–23, Jan. 2020.
[41] T. Tang, C. Wang, and M. Tomizuka, "A framework for manipulating deformable linear objects by coherent point drift," *IEEE Robot. Autom. Lett.*, vol. 3, no. 4, pp. 3426–3433, Oct. 2018.
[42] Z. Zhang, X. Wang, J. Liu, C. Dai, and Y. Sun, "Robotic micromanipulation: Fundamentals and applications," *Annu. Rev. Control, Robot., Auton. Syst.*, vol. 2, pp. 181–203, 2019.
[43] A. Billard and D. Kragic, "Trends and challenges in robot manipulation," *Science*, vol. 364, no. 6446, 2019, Art. no. eaat8414.
[44] F. Guerin and P. Ferreira, "Robot manipulation in open environments: New perspectives," *IEEE Trans. Cogn. Devel. Syst.*, vol. 12, no. 3, pp. 669–675, Sep. 2020.
[45] D. Q. Mayne, "Model predictive control: Recent developments and future promise," *Automatica*, vol. 50, no. 12, pp. 2967–2986, 2014.
[46] L. Shi, Y. Yuan, and J. Chen, "Finite horizon LQR control with limited controller-system communication," *IEEE Trans. Autom. Control*, vol. 58, no. 7, pp. 1835–1841, Jul. 2013.
[47] A. Escande, N. Mansard, and P.-B. Wieber, "Hierarchical quadratic programming: Fast online humanoid-robot motion generation," *Int. J. Robot. Res.*, vol. 33, no. 7, pp. 1006–1028, 2014.
[48] M. Majnik and Z. Bosnić, "ROC analysis of classifiers in machine learning: A survey," *Intell. Data Anal.*, vol. 17, no. 3, pp. 531–558, 2013.
[49] T. G. Cooper, "The epididymis, cytoplasmic droplets and male fertility," *Asian J. Androl.*, vol. 13, no. 1, pp. 130–138, 2011.
[50] D. Pandey, X. Yin, H. Wang, and Y. Zhang, "Accurate vessel segmentation using maximum entropy incorporating line detection and phase-preserving denoising," *Comput. Vis. Image Understanding*, vol. 155, pp. 162–172, 2017.
[51] J. M. Baltz, P. Oneeka Williams, and R. A. Cone, "Dense fibers protect mammalian sperm against damage," *Biol. Reproduction*, vol. 43, no. 3, pp. 485–491, 1990.
[52] H. Gadělha and E. A. Gaffney, "Flagellar ultrastructure suppresses buckling instabilities and enables mammalian sperm navigation in high-viscosity media," *J. Roy. Soc. Interface*, vol. 16, no. 152, 2019, Art. no. 20180668.
[53] P. A. Almeida and V. N. Bolton, "The effect of temperature fluctuations on the cytoskeletal organisation and chromosomal constitution of the human oocyte," *Zygote*, vol. 3, no. 4, pp. 357–365, 1995.

**Changsheng Dai** (Member) received the B.E. and M.E. degrees from the Harbin Institute of Technology, Harbin, China, in 2014 and 2016, respectively, and the Ph.D. degree from the University of Toronto, Toronto, ON, Canada, in 2020, all in mechanical engineering.

He is currently a Postdoctoral Fellow with the Advanced Micro and Nanosystems Laboratory, University of Toronto. His research interests include robotic cell manipulation and medical robotics.

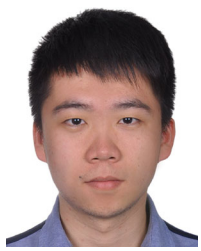

**Guanqiao Shan** (Graduate Student Member, IEEE) received the B.E. degree in electronic information engineering and the M.S. degree in physics from Beihang University, Beijing, China, in 2014 and 2017, respectively. He is currently working toward the Ph.D. degree in mechanical engineering with the University of Toronto, Toronto, ON, Canada.

His research interests include robotic cell manipulation and characterization.

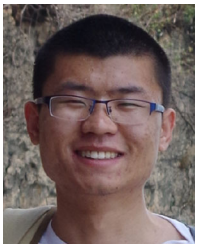

**Hang Liu** received the B.E. degree from Shanghai Second Polytechnic University, Shanghai, China, in 2014, and the M.E. degree from Shanghai University, Shanghai, in 2017, both in mechatronics engineering. He is currently working toward the Ph.D. degree in mechanical engineering with the University of Toronto, Toronto, ON, Canada.

His research interests include computer vision and medical image analysis.

**Changhai Ru** received the Ph.D. degree in mechatronics engineering from the Harbin Institute of Technology, Harbin, China, in 2005.

He was a Postdoctoral Fellow with the Department of Mechanical and Industrial Engineering, University of Toronto, Toronto, ON, Canada. He is currently a Professor with the School of Electronic and Information Engineering, Suzhou University of Science and Technology, Suzhou, China, and a Director of the JITRI Micro-Nano Automation System and Equipment Technology Research Institute. His research interests include microrobotics and nanorobotic manipulation, nanopositioning technology, and automated instrumentation for biomedical applications.

**Yu Sun** (Fellow) received the B.S. degree in electrical engineering from the Dalian University of Technology, Dalian, China, in 1996, the M.S. degree in control science and engineering from Institute of Automation, Chinese Academy of Sciences, Beijing, China, in 1999, and the M.S. degree in electrical engineering and the Ph.D. degree in mechanical engineering from the University of Minnesota, Minneapolis, MN, USA, in 2001 and 2003, respectively.

He is currently a Professor with the University of Toronto, Toronto, ON, Canada. He is a Tier I Canada Research Chair and Director of the Robotics Institute. His laboratory specializes in developing innovative technologies and instruments for manipulating and characterizing cells, molecules, and nanomaterials.

Dr. Sun was elected as Fellow of the American Society of Mechanical Engineers, the American Association for the Advancement of Science, the National Academy of Inventors, the Canadian Academy of Engineering, and the Royal Society of Canada for his work on micro–nano devices and robotic systems.